Finite-temperature modeling of nanoscale spin-transfer oscillators

S. E. Russek,* S. Kaka, W. H. Rippard, M. R. Pufall, and T. J. Silva

National Institute of Standards and Technology, Boulder, Colorado 80305, USA

(Received 29 September 2004; revised manuscript received 31 January 2005; published 31 March 2005)

Magnetization dynamics induced by spin-polarized currents in magnetic nanodevices have been numerically simulated using a single-domain model proposed by Slonczewski extended to include temperature effects. For currents with a spin polarization antiparallel to the device easy axis and for fields above the magnetostatic anisotropy field, transfer of spin momentum from one layer to an adjacent layer can cause the layers to undergo sustained oscillations. Here we numerically calculate the expected excitation spectra and linewidths of spin-transfer oscillators and explain observed variations in excitation linewidths. The linewidth arises from thermal excitations that give rise to disorder in the orbits and, in certain regimes, hopping between nearly degenerate orbits. The excitation spectra for a 2.5 nm × 50 nm × 100 nm device show transitions from thermally activated elliptical motion, at zero and low currents, to a bent elliptical motion at intermediate currents, and finally to tilted out-of-plane orbits. At the transition between in-plane and out-of-plane orbits, there is a region of low-frequency noise due to thermal hopping between degenerate orbits and a shift in the spectral behavior. The linewidth arising from thermal interactions is a sensitive function of the device volume and varies from 1 to 2 GHz for 2.5 nm × 50 nm × 100 nm devices to 20 to 40 MHz for 10 nm × 200 nm × 400 nm devices. The modeling explains the difference in linewidths observed for nanopillar and point-contact geometries as a natural consequence of inherent thermal fluctuations and the difference in excitation volumes.

I. INTRODUCTION

Dynamical excitations of the magnetization in small magnetic devices driven by large spin-polarized currents were predicted theoretically[1,2] and have recently been observed.[3,4] Direct observation of microwave output from small nanopillar and point-contact devices now allows for quantitative testing of proposed theoretical models. Extensive modeling of spin momentum transfer (SMT) effects have been made using a model proposed by Slonczewski that incorporates SMT effects into the Landau–Lifshitz (LL) equations of motion.[5–9] Here, we numerically study SMT effects using the single-domain Slonczewski model and extend previous studies by including effects of temperature and calculating observable excitation spectra. Finite temperature effects are important in determining the observed linewidth and understanding thermally activated switching between near-degenerate orbits. The modeling explains the large variation in linewidth observed in Refs. 3 and 4 as a natural consequence of the difference in excitation volumes. While the single domain simulations presented here cannot fully describe the induced dynamics in point contact devices, micromagnetic modeling of point contact spin-transfer oscillators (STOs) has shown that the area underneath the contacts behaves as a uniformly magnetized domain. The extent of the uniformly precessing region underneath the point contact is not currently known and the study presented here of intrinsic thermal linewidth in single domain STOs suggests that the effective excitation volume in the point contact STOs may be considerably larger than in the nanopillar STOs.

The device structure investigated was a current-perpendicular-to-plane (CPP) spin valve whose geometry is shown in Fig. 1. The device consists of two magnetic layers, a thinner free layer and a thicker reference layer, separated by a nonmagnetic spacer layer. A current is driven from the reference layer into the free layer, thereby transporting angular momentum (flow of electrons from the free layer into the reference layer is defined as a negative current). The equation of motion for the free-layer element, being driven by a spin-polarized current, is given by a modified LL equation[1]

$$\frac{d\vec{m}_1}{dt} = -\mu_0 \gamma \vec{m}_1 \times \vec{H}_{\text{eff}} - \mu_0 \gamma \alpha \vec{m}_1 \times (\vec{m}_1 \times \vec{H}_{\text{eff}})$$

$$+ \frac{\varepsilon I_{\text{inj}} \hbar}{e l_x l_y l_z 2} \frac{\gamma}{M_{s1}} \vec{m}_1 \times (\vec{m}_1 \times \vec{m}_2),$$

where $\vec{m}_1$ and $\vec{m}_2$ are the magnetizations of the free and reference elements normalized by the saturation magnetization M_s, $\vec{H}_{\text{eff}}$ is the effective field, γ is the gyromagnetic ratio, α is the Gilbert damping parameter, I_{inj} is the applied current, ε is an efficiency factor, e is the electron charge, and l_x, l_y, l_z are the device dimensions. The effective field is the sum of the applied field $\vec{H}_a$, the demagnetizing field $\vec{H}_{dm}$
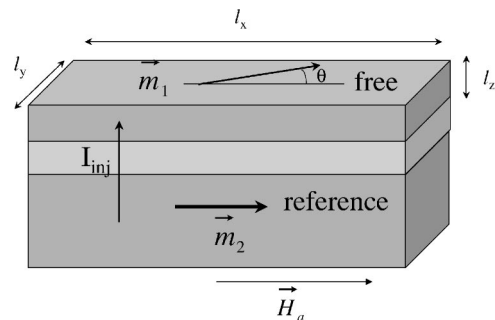
FIG. 1. Device schematic showing the free and reference layers, device dimensions, current direction, and applied field direction.
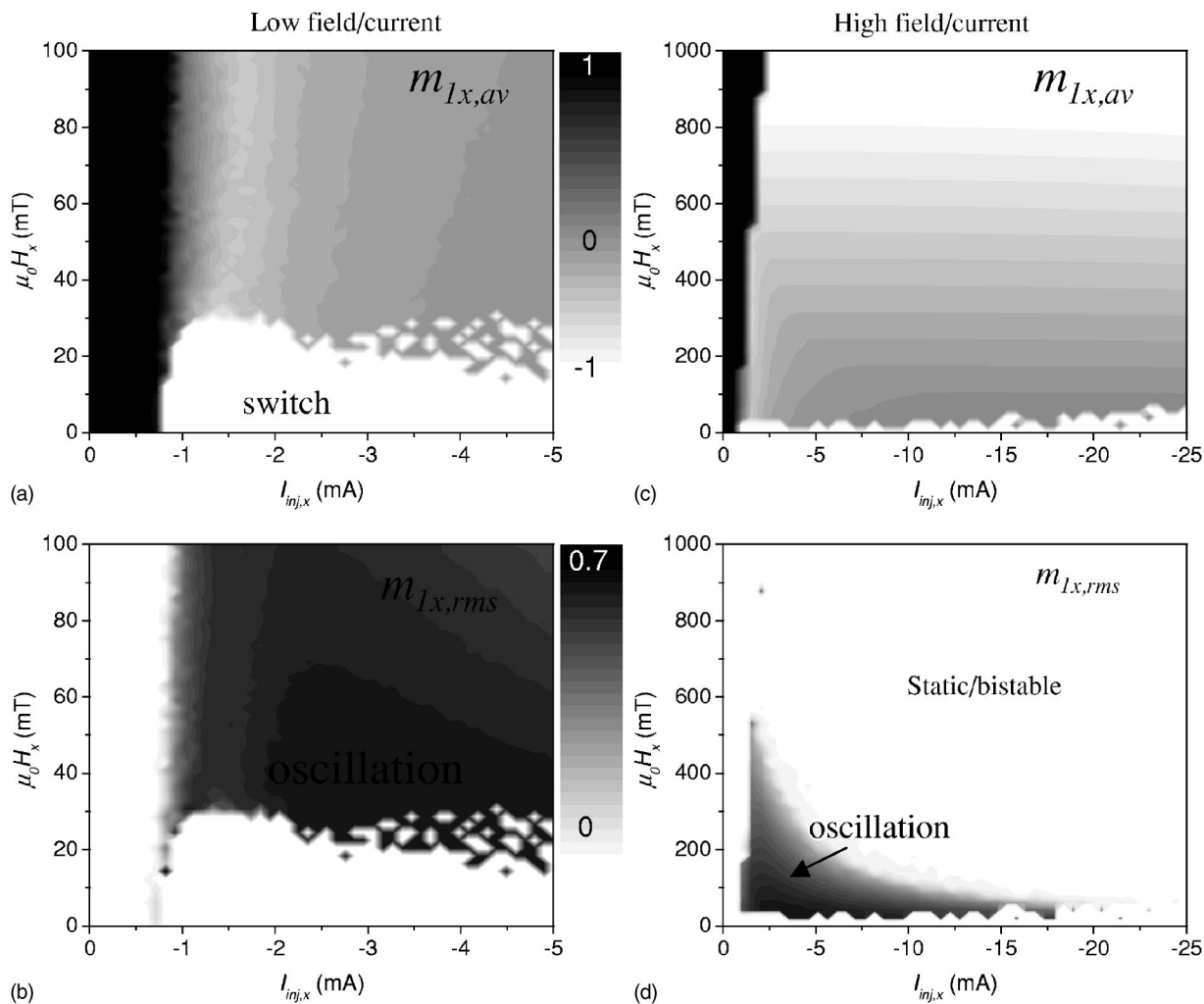
FIG. 2. (a) Simulated low-field phase diagram for a 2.5 nm × 50 nm × 100 nm device showing the steady-state values of $m_{1x,av}$ for a range of fields applied along the positive x direction, and current with polarization along the negative x direction. (b) Simulated phase diagram showing the steady values of $m_{1x,rms}$ for the same range of fields and currents. (c) and (d) are phase diagrams similar to (a) and (b) except at higher fields and currents.

$=M_s \bar{\bar{N}} \vec{m}_1$ (where $\bar{\bar{N}}$ is the demagnetizing tensor), and a thermal field $\vec{H}_{th}$. The demagnetizing field is determined from calculated demagnetizing factors for rectangular parallelepipeds,[10] and the thermal field is a random field with an rms value given by $\mu_0 H_{th,rms} = \sqrt{2kT\alpha / l_x l_y l_z M_s \gamma \Delta t}$, where T is the temperature and Δt is the period over which the thermal field is applied.[11] There are fluctuations in the applied current due to Johnson noise, which we neglect here and in practice, there are additional interaction fields between the two layers, which we also neglect. The efficiency factor ε is taken to be 0.2 for all of the simulations in this paper, a value consistent with previous experimental measurements.[12] We assume ε is a constant, independent of the angle θ between $\vec{m}_1$ and $\vec{m}_2$. In general, ε is dependent on θ and the dependence is a complicated function of the spin-dependent reflection and transmission factors for electrons at the magnetic-nonmagnetic interfaces.[13] The detailed dependence of the efficiency on angle is expected to change the details of the excitation dispersion relation but not the

qualitative behavior. The data shown in this paper are for a device with a free layer $M_{s1} = 800$ kA/m, $\alpha = 0.01$, and $T = 300$ K. The reference layer is rigidly fixed along the positive x direction. For most devices in a large field, the reference layer will be fixed along the field direction, and the giant magnetoresistance output voltage will be proportional to the component of the free layer magnetization along the field direction. Hence, for the geometry considered here, $m_{1x}(f)$ should be proportional to the measured voltage spectrum. In the calculations, the equations of motion were integrated to 30 to 50 ns. The typical integration time step was <5 fs.

A phase diagram can be constructed by integrating the equations of motions for a range of applied currents and magnetic fields and calculating the values of $m_{1x,av} = \langle m_{1x}(t) \rangle$ and $m_{1x,rms} = \{\langle [m_{1x}(t) - \langle m_{1x} \rangle]^2 \rangle\}^{1/2}$ after the system reaches a steady state. Plots of $m_{1x,av}$ and $m_{1x,rms}$, as a function of easy axis field H_{ax} and injection current $I_{inj,x}$, are shown in Fig. 2 for a 2.5 nm × 50 nm × 100 nm device in the low field (a), (b) and high field (c), (d) regions. These dia-

grams are in general agreement with similar phase diagrams discussed in Refs. 3 and 9. The device starts in the $m_{1x}=1$ state. For applied fields below the magnetostatic anisotropy field, $\mu_0 H_k = H_{dm,y} - H_{dm,x} = 33$ mT, the magnetization will switch to the $m_{1x}=-1$ state at a threshold current of ≈ 1 mA. There are no sustained oscillations in this region, given $m_{1x,rms}=0$. For larger applied fields, the free-layer magnetization will be driven into an oscillating state above the threshold current. The regions of oscillations decrease as the applied field increases until it exists only in a very narrow region of applied currents. The oscillation amplitude can be quite large, $m_{1x,rms}=0.7$, predicting that the voltage output signal should be a substantial fraction of $I\Delta R$, where ΔR is the change in resistance between the parallel and antiparallel states. The boundary between the oscillating and the static switched state is blurred by thermal effects. Near this boundary, the device spends part of the time in a static state and part of the time in a precessional state.

At large applied fields and currents [in the region labeled "static/bistable" in Fig. 2(d)], the magnetization evolves into a static state in which the magnetization is canted in the negative x direction. The system is bistable and can end up in a state with negative m_y and m_z or positive m_y and m_z. For instance, with $\mu_0 H_{ax}=0.8T$ and $I_{inj,x}=-15$ mA the stable states are $m_x=-0.93$, $m_y=-0.044$, $m_z=-0.38$ or $m_x=-0.93$, $m_y=0.044$, $m_z=0.38$.

II. EXCITATION SPECTRA

The calculated excitation spectra (the average magnitude of the Fourier transform of the magnetization) for a device at $T=300$ K and $\mu_0 H_a = 50$ mT are shown in Figs. 3(a) and 3(b). The data are obtained by averaging the magnitude of the Fourier transforms of the steady-state magnetization trajectories of 10 numerical simulations that differ only in the stochastic variation from the thermal field term. The spectral maps are plotted on a logarithmic scale to make small-scale excitations, such as thermal excitations and higher harmonics of SMT oscillations, visible. The excitation trajectories are shown in Figs. 3(c)–3(e). At low bias currents, the magnetization is driven by the thermal fields, and the excitation spectra are just the thermal magnetic noise. These excitations appear as disordered elliptical precession, seen in Fig. 3(c), at the ferromagnetic resonant (FMR) frequency and are similar to those observed in current-in-plane (CIP) spin valves.[14] The simulated resonant frequency, 7.76 GHz, is close to the resonance frequency predicted by the Kittel relation[15] $f_r = \mu_0 \gamma \sqrt{H_y H_z} = 7.77$ GHz, where $H_y = H_k + H_a$ and $H_z = (N_{zz} - N_{xx})M_s + H_a$ are, respectively, the stiffness fields in the y and z directions. In this region, where the excitations are small, the motion of m_{1x} is frequency doubled and is much smaller in amplitude than the fluctuation in m_{1y}, since $m_{1x} \propto \cos\theta \approx 1 - \frac{1}{2}\theta^2$. As the current increases, the SMT term drives larger excitations at the FMR frequency, as seen in Fig. 4. The excitation linewidth is shown in the inset of Fig. 4 for low current values. The zero-current linewidth is expected to be proportional to the square root of the imaginary part of the magnetic transverse susceptibility, which for small excitations can be expressed in closed form. The ex-

pected full-width-at-half-maximum (FWHM) linewidth,[11] $\Delta f = 1.55\alpha\mu_0\gamma(H_y + H_z) = 0.44$ GHz, is close to the simulated low-current linewidth. Here, the factor of 1.55 occurs because the expected linewidth is proportional to the square root of the susceptibility, not the susceptibility. The magnitude of the excitations increase as the spin-polarized current increases and the linewidth decreases, which indicates that the SMT term in the LLG equation, for this limited range of motion, acts as if it decreases the damping constant.

Above a threshold current, the device goes into sustained SMT-driven oscillations. A trajectory for -1 mA injection current is shown in Fig. 3(d). The SMT term pushes the trajectory toward the negative x direction. This extension of the trajectory with increasing injection current causes the oscillation frequency to initially decrease, as seen in Figs. 3(a) and 3(b). Thermal fluctuations give rise to a distribution of orbits with different frequencies that gives rise to the excitation linewidth. For the -1 mA trajectory, the first harmonic linewidths for m_{1x} and m_{1y}, as seen in Fig. 5(a), are 0.85 GHz and 2.1 GHz, respectively, which is considerably broader than the FMR linewidth. As the injection current is further increased and the excursions in the magnetization approach the $-x$ direction, the orbit will intersect itself and will bifurcate into two out-of-plane orbits as seen in Fig. 3(e). At this point the oscillation frequency goes through a minimum, and the linewidth gets broad since thermal activation now causes the system to switch between three nearly degenerate orbits. As the injection current is increased further, the system settles into one of the out-of-plane orbits. As the injection current increases these orbits move out of plane, decrease in amplitude, and increase in frequency.

None of the SMT-induced orbits are perfectly harmonic, and higher-order peaks are visible. For the $I_{inj}=-1$ mA orbit, the first and third harmonics are visible in the m_{1y} spectra and the second and fourth harmonics are visible in the m_{1x} spectra shown in Fig. 5(a). The ratios of the harmonic amplitudes provide a good test when comparing to experimental data to determine whether the observed spectra correspond to the excitation predicted by these models. While the spin-current-induced orbits are relatively insensitive to small deviations of the spin momentum direction from the free layer easy axis, the observed signal, which is proportional to the component of the magnetization along the spin momentum direction, is very sensitive. When there is a misalignment the observed spectra will contain components of m_{1y} spectra, in addition to the m_{1x} spectra, and will lead to a mixing of even and odd harmonic components, as seen in Fig. 5(b) for the case of a 20° misalignment. This mixing leads to an angle dependent variation of the harmonic amplitudes. There is also a small increase in the precessional frequency due to a change in the orbit as the injected spin axis deviates from the device easy axis and the applied field direction.

The linewidths of the SMT-induced excitations are a function of the dispersion relation df_r/dH_a and the thermal field. We expect a broader linewidth when df_r/dH_a or H_{th} is large. Conversely, when the device temperature is small or the device volume is large, H_{th} and hence the linewidth will be small. The linewidths for a series of scaled devices are shown in Fig. 6. Here, all of the device dimensions are scaled by a factor η (the volume increases as η^3) and the
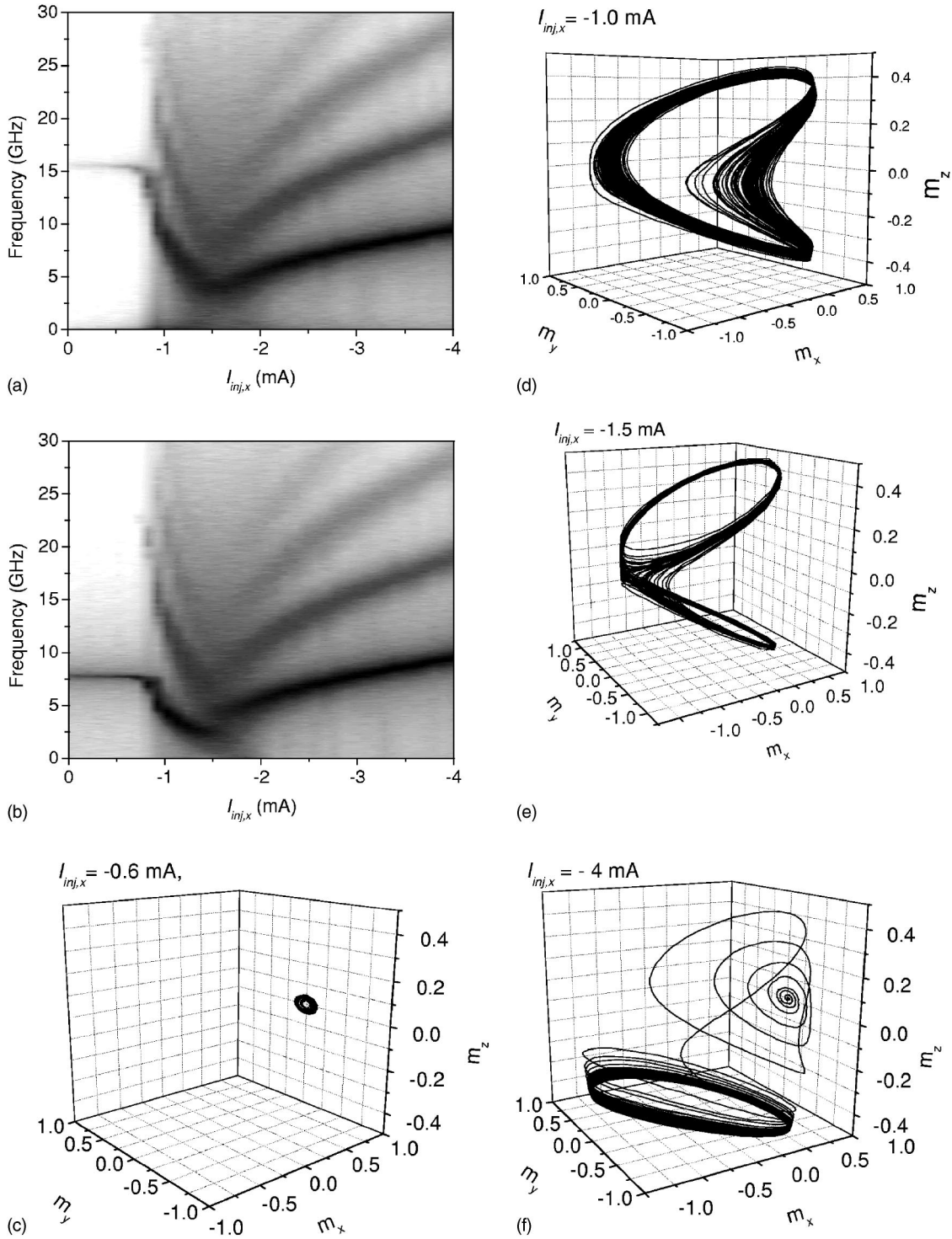
FIG. 3. Excitation spectra at 300 K for a 2.5 nm × 50 nm × 100 nm device as a function of spin polarized injection current for an applied *x*-axis field of 50 mT: (a) $m_{1x}(f)$ excitation spectra, (b) $m_{1y}(f)$ excitation spectra. The excitation spectra are plotted on a logarithmic scale with white indicating $m(f) < 0.001$ and black indicating $m(f) = 0.5$. (c), (d), (e), and (f) show the calculated trajectories for $I_{inj,x} = -0.6$, $-1.0, -1.5$ mA, and -4.0 mA, respectively. (f), in addition to the final stable orbit, shows the time evolution from the initial state.

injection current is scaled by a factor η^3. The injection current is $I_{inj,x} = 1$ mA for the 100 nm device and 64 mA for the 400 nm device. The magnetostatic fields and the SMT trajectories, in the absence of thermal fluctuations, are identical for all of the simulations. The excitation linewidth decreases rapidly with device volume and decreases from 1 to 2 GHz

for an $l_x = 100$ nm device to 20 to 40 MHz for an $l_x = 400$ nm device. The decrease in linewidth is approximately exponential with a decay length of 82 nm. This decrease in linewidth for the large angle SMT excitations is in contrast to the H_{th}-independent linewidth observed for small angle FMR excitations.
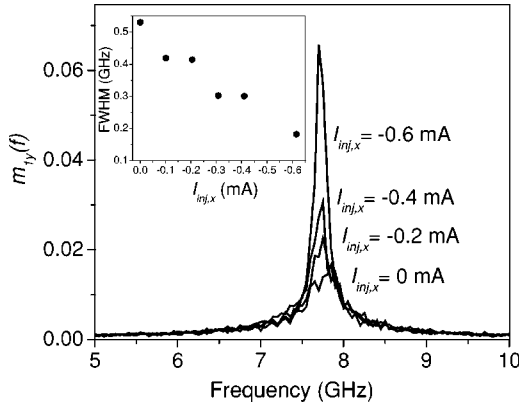
FIG. 4. Excitation spectra $m_{1y}(f)$ for low values of injection current (in the thermal FMR regime) at an applied x-axis field of 50 mT and temperature of 300 K showing an increase in amplitude and a decrease in linewidth as the current increases. The inset shows the resonant linewidth as a function of injection current.

III. DISCUSSION

The modeling indicates that the SMT-induced excitations grow naturally out of the thermally driven small angle FMR excitations. As the SMT term drives in-plane precession, there will be an initial decrease in resonant frequency, or a redshift, with increasing current. When the bent in-plane orbit becomes degenerate with the out-of-plane orbit there is considerable low frequency noise due to the jumping of the trajectory from in-plane to out-of-plane orbits. At high currents, when the orbits are out of plane, the resonant frequency increases with applied current (blueshift). The width of the resonance is quite broad due to thermal agitation and the small size of the device. This type of thermal broadening must be present in any magnetic device that is in contact with a thermal heat bath. However, there may be other effects, such as inhomogeneous magnetostatic fields and defects, that may lead to additional temperature-independent broadening. The thermal effects discussed here determine a lower limit on the excitation linewidth. The predicted linewidth depends exponentially on the thermal field and increases with increasing temperature or decreasing device volume. Thus, the coherent oscillation volume must be relatively large if one desires a narrow linewidth.

In comparison with experimental data from Refs. 3 and 4, the model qualitatively predicts certain features that are observed in SMT-induced excitations. The point-contact data in Ref. 4 show a redshift for in-plane orbits and a transition to a blueshift when the excitation is driven out of plane. The blueshift, however, is most often observed when the field has an out-of-plane component and the structure shown in Fig. 3 for in-plane fields is not always observed. The observed linewidths for the nanopillar devices in Ref. 3 are typically on the order of 1 GHz at room temperature, consistent with the predictions of the calculated spectra. The linewidths of point contact devices are on the order of 20 MHz, which is consistent with an increased excitation volume due to the generation of an extended spin wave. The calculated excitation volume of 400 nm is comparable to the wavelength of the excited spin waves as determined by fitting the frequency vs
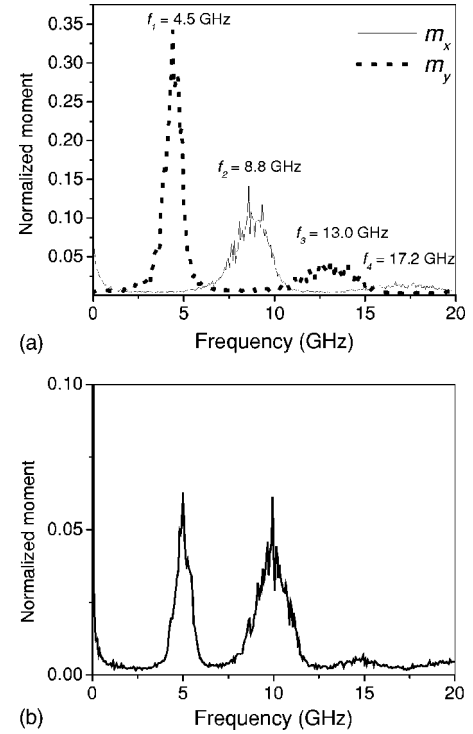
FIG. 5. (a) Excitation spectrum $m_{1x}(f)$ and $m_{1y}(f)$ for $I_{inj,x}$ =−1 mA showing spectra for an SMT driven precessional orbit for a applied x-axis field of 50 mT and a temperature of 300 K. The fundamental and third harmonic peaks are seen in $m_{1y}(f)$, and the second and fourth harmonics are seen in $m_{1x}(f)$. (b) Calculated excitation spectra for the case when the reference layer magnetization is fixed 20° off the easy-axis direction and $I_{inj,x}$=−0.94 mA, $I_{inj,y}$=−0.34 mA. The excitation spectra is the Fourier transform of the component of the free-layer magnetization along the reference layer.

field data.[4] Other observed features cannot be described by this simple single-domain model. These features include sudden jumps in the excitation spectra with applied field or current and the presence of regions of broad-band instability. Many important effects have been ignored in the present cal-
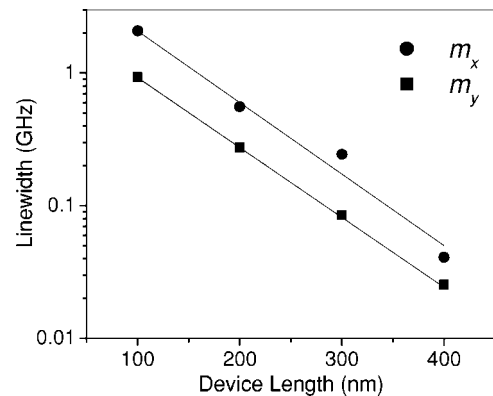
FIG. 6. Linewidth of m_{1x} and m_{1y} excitations for a applied x-axis field of 50 mT and a temperature of 300 K as a function of device length l_x. All dimensions are scaled simultaneously so that the aspect ratio remains constant. The lines are exponential fits, which yield a decay length of 82 nm.

culations such as micromagnetic structure, current-generated magnetic fields, motion of the fixed layer, and angle dependent efficiencies and damping. The details of the current-induced precessional orbits are expected to differ in real devices compared to the single-domain simulations. However, the dependence of the linewidth on temperature and excitation volume should be qualitatively similar when these additional effects are included. This implies that to obtain practical room-temperature spin-transfer oscillators with narrow linewidths ($Q > 10\,000$) we will require large excitation volumes (diameters > 400 nm) and a flat dispersion region (small df_r/dH_a).

---

*Author to whom correspondence should be addressed. Electronic address: russek@boulder.nist.gov

[1] J. C. Slonczewski, J. Magn. Magn. Mater. **159**, L1 (1996).

[2] L. Berger, Phys. Rev. B **54**, 9353 (1996).

[3] S. I. Kiselev, J. C. Sankey, I. N. Krivorotov, N. C. Emley, R. J. Schoelkopf, R. A. Buhrman, and D. C. Ralph, Nature (London) **425**, 380 (2003).

[4] W. H. Rippard, M. R. Pufall, S. Kaka, S. E. Russek, and T. J. Silva, Phys. Rev. Lett. **92**, 027201 (2004).

[5] J. Z. Sun, Phys. Rev. B **62**, 570 (2000).

[6] Z. Li and S. Zhang, Phys. Rev. B **68**, 024404 (2003).

[7] X. Zhu and J-G Zhu, J. Appl. Phys. **95**, 7318 (2004).

[8] Ya. B. Bazaliy, B. A. Jones, and S.-C. Zhang, Phys. Rev. B **69**, 094421 (2004).

[9] H. Xi and Z. Lin, Phys. Rev. B **70**, 092403 (2004).

[10] A. Aharoni, J. Appl. Phys. **83**, 3432 (1998).

[11] J.-G. Zhu, J. Appl. Phys. **91**, 7273 (2002).

[12] W. H. Rippard, M. R. Pufall, and T. J. Silva, Appl. Phys. Lett. **82**, 1260 (2003).

[13] Jiang Xiao, A. Zangwill, and M. D. Stiles, Phys. Rev. B **70**, 172405 (2004).

[14] N. Stutzke, S. L. Burkett, and S. E. Russek, Appl. Phys. Lett. **82**, 91 (2003).

[15] C. E. Patton, in *Magnetic Oxides*, edited by D.J. Craik (Wiley, New York, 1975), pp. 575–647.